CHAPTER III. INSTRUMENT CHARACTERIZATION

III.1.-- INITIAL INSTRUMENT OPERATION

Simple samples such as pure metals were analyzed to investigate the properties of the new LI-TOF-MS instrument. Metal foils (tungsten, indium) and an aluminum disk were chosen primarily for their ease of mass identification; only a single m/z peak (or isotopic distribution) should dominate the mass spectrum. Various instrumental parameters such as the ion focussing lens, horizontal and vertical deflection plates, and acceleration (flight tube) potentials were varied to see the effect of these parameters on the spectrum. Furthermore, the ion extraction procedure was systematically investigated to probe the effects of the extraction (repeller) voltage, extraction pulse delay time, and width of the pulse.

Initial characterization was performed with a 1-mm thick disk of pure tungsten foil while operating the TOF-MS in linear mode, which eliminated the reflectron voltages from the variable parameters. Choosing basis parameters of “neutral” (0 Volts) ion lens and deflection plate potentials, a detector gain of –2000 Volts, and a flight tube voltage of –2000 Volts (startup parameters as specified by the manufacturer), the ion extraction “repelling” process was studied. A constant DC extraction potential of +200 Volts was applied to the repeller plate, but this yielded only a broad (~6 μsec) signal in a total time of flight of approximately 40 μsec.

The preferred method of operation employs a delayed, pulsed extraction. The “repeller delay” introduces additional parameters into the extraction process, and first a suitable “delay time” must be determined. This extraction pulse delay, calculated from the laser fires to the time of the extraction voltage pulse, allows the tungsten ions to rise from the sample surface to the flight tube axis before repelling the ions in a concentrated packet into the flight tube. In addition, the width of the extraction pulse could be adjusted to elongate the duration of the voltage. Figure II.5 from chapter II summarizes these events.

With an extraction voltage of +200 V, the delay time and pulse width were slowly and individually manipulated until an optimal delay was determined to be 21.5 μsec. Operating too far outside of approximately a 3-μsec window from this delay time yielded little signal. The effect of the extraction pulse width was much less crucial, with little impact on the intensity and resolution of the ion peak. Widths greater than about 5 μsec generated little signal, leading to the conclusion that the long pulse width effectively simulated the constant DC extraction mode and therefore provided only a broad ion packet into the flight tube. In addition, pulse widths under about 0.5 μsec did not extract enough ions from the source region into the flight tube to provide a significant signal. The pulse width chosen as optimal was 2.0 μsec; however, widths between 1.0 and 3.0 μsec provided little differences on the observed spectrum.

Once the extraction parameters were set, the deflection plates (horizontal and vertical) and the ion lens potentials were optimized. Remaining in linear mode, however, afforded only extremely broad ion peaks of over 1 μsec FWHM in a 40-μsec time-of-flight, and varying the instrumental parameters could not decrease this peak width significantly. Therefore, it was clear that the laser ablation process produced such a wide range of initial kinetic energies of the ablated tungsten ions that operation in the reflectron mode was necessary to correct for this problem. Only by using the reflectron could the other parameters be investigated thoroughly.

For the reflectron mode of operation, a higher extraction potential was employed (+300 V instead of +200 V) for resolution improvement, while the flight tube potential was held at –2000 V. The voltages for the two reflectron lenses were varied continually until signals were observed in the time-of-flight spectrum while using the detector located after the secondary flight tube. Due to the second-order focussing capabilities of the dual stage reflectron, the lens potentials were changed together slowly until a tungsten ion signal was observed and experimentally improved. Conditions were optimized experimentally (for a fixed acceleration voltage of –2000 V) at –1000 V on the front lens and +700 V on the rear lens. Resolution improvement was substantial at over 25 times the linear mode (~20 vs. ~500) for the tungsten isotopes.

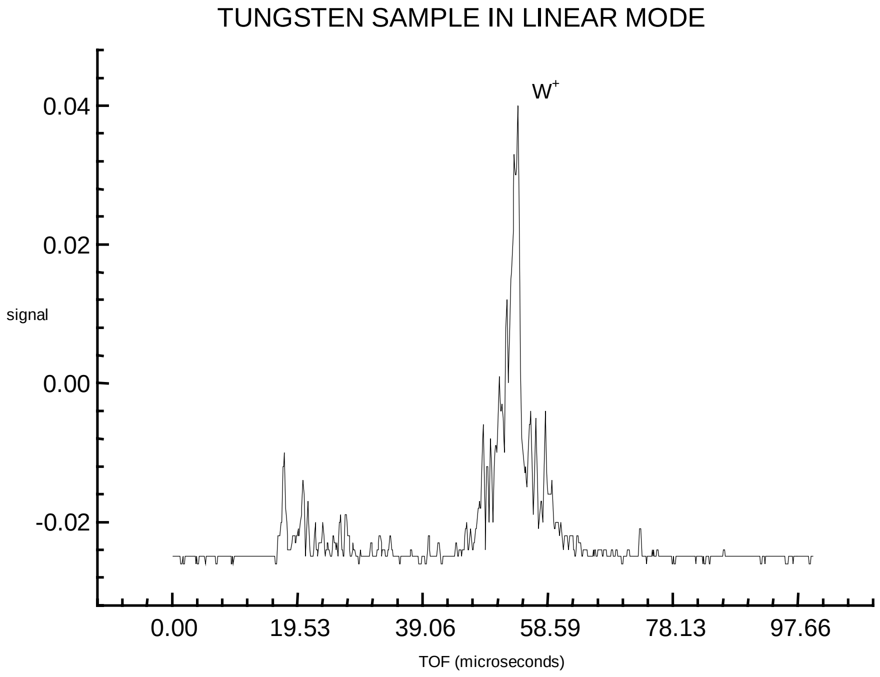

Figure III. 1: Linear mode instrument operation--Poor resolution for the W$^+$ ion.

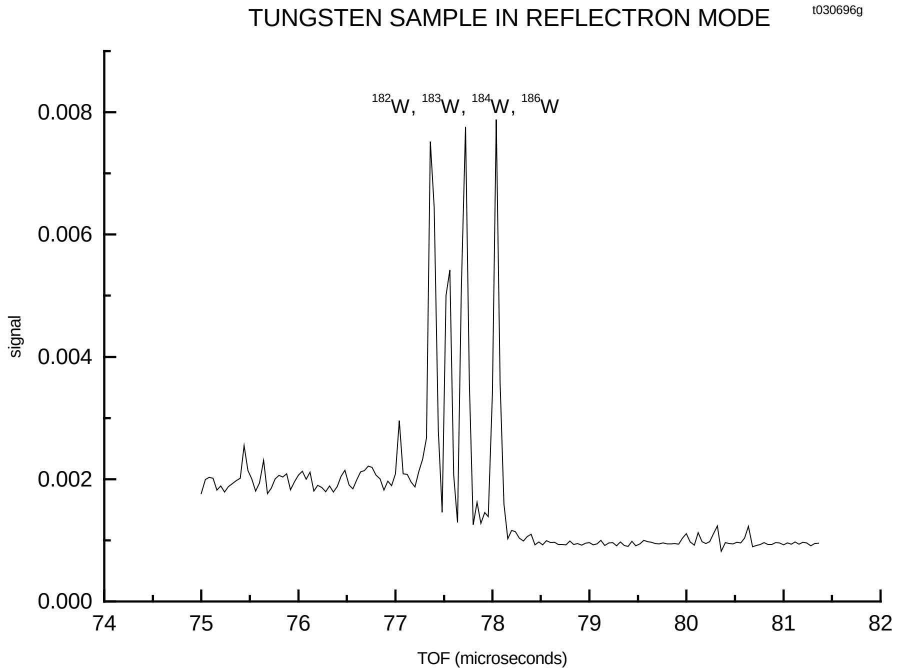

Figure III. 2: Reflectron mode of instrument operation-- Distinct resolution of all W$^+$ isotopes.

A comparison of the linear (Figure III.1) and reflectron (Figure III.2) spectra illustrates the importance of the kinetic energy correction with the reflectron. Further studies with the indium and aluminum samples confirmed that the laser ablation process imparts large initial kinetic energy variations for all samples.

III.2.-- REPRODUCIBILITY OF EXPERIMENTAL TIMES-OF-FLIGHT

Under a given set of extraction, acceleration, and reflectron potentials, the time-of-flight of a given ion must remain constant to ensure accurate data. Again, the tungsten foil was analyzed to determine the reproducibility of the times-of-flight of the ions. Spectra were recorded as the average of 100 laser shots, and the corresponding time-of-flight (measured at the peak maximum of the centroid) was pinpointed. As is shown in Table III.1, the times-of-flight of each isotope are reproducible to within 0.01% relative standard deviation (%RSD). This concrete example is typical of what is observed regularly with our instrument. The minimal differences could possibly be attributed to electronics and triggering jitter, but it is clear that the time-of-flight for any ion is highly reproducible. These consistencies confirm proper instrumental operation and lend credence to all mass spectral data.

III.3.-- SPACE FOCUS

III.3.1.-- Primary (first-order) space focus

Another monoelemental sample, an aluminum disk (5/8-inch diameter, 1/8-inch thick), was chosen to investigate the space-focusing conditions of the dual-source extraction of our system more thoroughly. In addition to its single-element simplicity, aluminum was used in this analysis for its mono-isotopic (27 amu) natural abundance. Therefore, these single-peak mass spectra could be analyzed in a straightforward manner without concern for isotopic resolution.

Because of the poor quality of linear spectra, the reflectron was employed to investigate the space focus for both the first- (primary) and second-order space focusing conditions. Although linear mode operation assesses the first-order focus directly, experimental peak widths could not be significantly influenced to thoroughly study the relation between the extraction and acceleration potentials. This again highlights the

Table III. 1: Reproducibility of tungsten isotope times-of-flight.

SPECIES	$^{182}W^+$	$^{183}W^+$	$^{184}W^+$	$^{186}W^+$
TIME	60.79	60.95	61.12	61.45
OF	60.80	60.96	61.14	61.46
FLIGHT	60.80	60.96	61.14	61.46
(μs)	60.80	60.96	61.14	61.44
	60.78	60.95	61.11	61.46
	60.80	60.97	61.13	61.46
	60.79	60.96	61.13	61.46
	60.79	60.96	61.14	61.46
	60.79	60.96	61.14	61.46
MEAN (μs)	60.79	60.96	61.13	61.46
%RSD	0.012%	0.010%	0.018%	0.012%

wide kinetic energy distribution generated by our ablation process. Although sources disagree[43], Boesl[44] suggests that an approximation of the first-order focus can be made by placing this point near the beginning of the reflectron. Thus, by keeping the reflectron parameters constant while varying the extraction (E_s) and acceleration potentials (E_d), the primary space focus was evaluated for our TOF-MS and its effects on the spectra were observed.

Two measurements, the peak width (FWHM) and intensity, gauge the quality of the spectra and thus the focusing. The peak width assesses the resolution, or narrowness of the ion packet, which strikes the detector. Since resolution and FWHM are inversely related, the best spectra will minimize the FWHM to display the narrowest, sharpest peak. Numerical evaluation of the width (nanoseconds) and intensity (mV) were obtained directly from the oscilloscope. Quite obviously, the maximum intensity is

---

[43] B.A. Mamyrin. *Int. J. Mass Spectrom. Ion Processes.* **131** (1994) 1.

[44] U. Boesl, R. Weinkauf, E. Schlag. *Int. J. Mass Spectrom. Ion Processes.* **112** (1992) 121.

desired for the best sensitivity and instrument optimization. Although an accurately integrated peak area is the most indicative assessment of the ion yield, this calculation is difficult and can only be reliably performed after importing the entire spectrum into a spreadsheet program for evaluation. Thus, an approximation of the ion yield, given by the peak height, was employed in this investigation. Ten spectra of 100 laser shots each were averaged for each set of conditions. For experimental simplicity, only the most common acceleration voltages (-2000 V to -2400 V) were used for the investigation. Previous experimentation revealed that for these acceleration potentials, extraction voltages between +100 V and +400 V provided a significant ion signal. Operating outside of these extraction potentials afforded little detectable signal. In an extreme case, the signal intensity was so low (under 0.50 mV) that the signal characteristics for high repeller potentials were omitted from the -2000 V acceleration voltage data series. Table III.2 highlights the quality of the Al^+ peak as a function of the acceleration and extraction potentials.

A plot of the FWHM and peak intensity for each acceleration voltage, as shown in Figure III.3, clearly depicts the changing optimal extraction potential for each acceleration voltage. In general, the lower acceleration potentials demand a lower extraction potential to achieve the best peak characteristics. In addition, analysis of Table III.2 shows that both the intensity and resolution maximize near the same extraction potential for a given acceleration voltage. Hence, correcting for the initial spatial distributions of the ions in the source region maximizes both the sensitivity and resolution of the measurement simultaneously.

From theoretical principles and a precise knowledge of the geometry of the instrument, the space focus conditions can be found for a dual-field (extraction and acceleration) configuration such as ours according to the Wiley-McLaren space focus relation (Equation I.15 of chapter I).

Table III. 2 : Primary space focus investigation-- dependence of spectral characteristics on the extraction (repeller) and acceleration (flight tube) potentials of the Al^+ peak from the aluminum sample.

ACCELERATION POTENTIAL -2000 Volts

Repeller Voltage (+V)	MEAN Resolution (FWHM in ns)	MEAN Intensity (mV)
400		
375		
350		
325	350	0.80
300	273	0.90
275	255	0.80
250	213	0.83
225	169	0.90
200	95	1.20
175	98	1.00
150	108	0.97
125	135	0.93
100	135	0.85

ACCELERATION POTENTIAL -2100 V

Repeller Voltage (+V)	MEAN Resolution (FWHM in ns)	MEAN Intensity (mV)
400	365	1.37
375	302	1.37
350	252	1.17
325	210	1.37
300	147	1.33
275	97	1.43
250	85	1.77
225	78	1.77
200	83	1.80
175	99	1.53
150	137	1.37
125	150	1.30
100	215	1.17

ACCELERATION POTENTIAL -2200 Volts

Repeller Voltage (+V)	MEAN Resolution (FWHM in ns)	MEAN Intensity (mV)
400	158	1.63
375	148	1.70
350	120	1.73
325	82	2.10
300	80	2.27
275	81	2.47
250	75	2.43
225	83	2.17
200	107	2.17
175	135	1.93
150	188	1.83
125	247	1.67
100	322	1.47

ACCELERATION POTENTIAL -2300 V

Repeller Voltage (+V)	MEAN Resolution (FWHM in ns)	MEAN Intensity (mV)
400	105	2.37
375	95	2.43
350	88	2.53
325	70	2.53
300	83	2.40
275	80	2.63
250	93	2.63
225	105	2.60
200	135	2.47
175	175	2.20
150	228	2.27
125	288	2.07
100	347	1.93

ACCELERATION POTENTIAL -2400 Volts

Repeller Voltage (+V)	MEAN Resolution (FWHM in ns)	MEAN Intensity (mV)
400	95	2.70
375	92	2.83
350	88	3.03
325	88	3.13
300	92	3.27
275	107	3.13
250	138	3.10
225	157	2.90
200	183	3.00
175	223	2.43
150	263	2.40
125	320	2.00
100	387	1.93

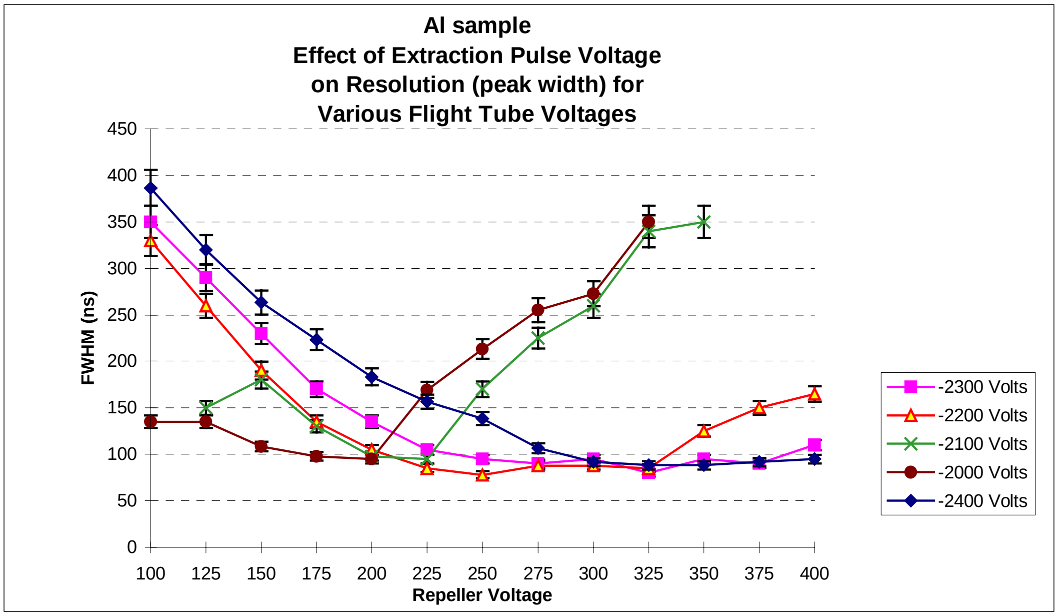

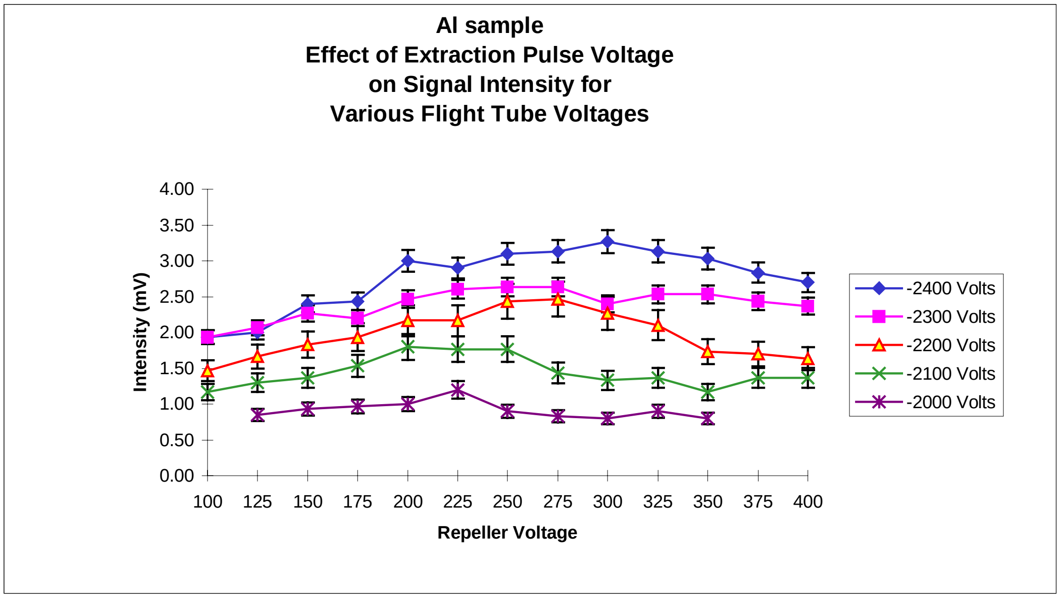

Figure III. 3: Primary space focus investigation-- dependence of spectral characteristics on the extraction (repeller) and acceleration (flight tube) potentials of the Al^+ peak from the aluminum sample.

However, in practical operation, the two potentials, E_d and E_s, are adjusted in a trial-and-error manner to find the best ratio (E_d/E_s) to achieve the space focus. By experimental rather than purely theoretical adjustments, correction for uncertainties in factors such as the exact location of ionization, s_0, (due to laser spot size) and an inexact knowledge of the instrumental configuration (d, s, D) will be eliminated. In addition, improvements minimizing other resolution-limiting factors such as the turn-around-time, space-charge effects, and time of ion formation can be attained. A comparison of the theoretical and experimental determinations might even reveal sources of peak broadening. Using the space focus equation, we see in Table III.3(a) that the experimental distance depends highly on the approximation of the mean position (s_0) of ion formation. In all cases, the experimental focus distances are less than the theoretical distance of our linear flight tube (D = 1 meter). Thus, k_0 in Equation I.15 of chapter I is larger than expected due to a high extraction voltage (i.e. E_s is high). Recalling that high extraction fields aid in minimizing non-spatial factors such as space-charge effects, turn-around-time, etc, it is likely that these other causes contribute greatly to the peak broadening in our LI-TOF-MS.

A further analysis of the data also looks at the second derivative of time as a function of the mean initial ion position, as given by Equation I.17 of chapter I. For all of our s_0 approximations, the second derivative reveals a maximum since the right side of the equation $\{(k_0-3)/k_0 \times D/s_0\}$ is greater than the left (d/s_0). Thus, $\partial^2T/\partial s_0^2 > 0$, and the preferred mode of operation to maximize the time-of-flight[45], was achieved in our experiments (See Table III.4).

Again referring to the space focus equation, the primary space focus is theoretically independent of the particular ion investigated, as was mentioned in chapter I. This independence is advantageous since instrumental conditions can be optimized for one mass and then used for complex mixture analysis. However, other factors affecting resolution which are mass-dependent will not be corrected.

In an effort to confirm the mass-independence of the space focus, a 2-mm thick pellet of a doped metal oxide, 0.033% Eu:CaO, was used in the same investigation (except that the minimum acceleration potential used was –2100 Volts). The abundant

---

[45] W.C. Wiley, I.H. McLaren. *Rev. Sci. Instrum.* **26** (1955) 1150.

Table III.3 (a) and (b): Optimized Acceleration and Extraction potentials for first-order space-focusing.

(a) Aluminum ion of the pure aluminum sample			
Acceleration Voltage (V_d)	**Extraction Voltage (V_s)**	**Ratio: V_d/V_{total}**	**Ratio: E_d/E_s**
2000	225	0.91	10.00
2100	225	0.90	9.33
2200	275	0.89	8.00
2300	325	0.88	7.08
2400	350	0.87	6.86

(b) Calcium oxide ion of the 0.033%Eu:CaO sample			
Acceleration Voltage (V_d)	**Extraction Voltage (V_s)**	**Ratio: V_d/V_{total}**	**Ratio: E_d/E_s**
2100	225	0.90	9.33
2200	250	0.90	8.80
2300	325	0.88	7.08
2400	350	0.87	6.86

Table III. 4 : Primary space focus investigation-- calculated space focus distances (D) for the optimized extraction (V_s) and acceleration (V_d) potentials using the Wiley-McLaren space focus equation.

s = d = 1.35cm
Take optimized V_d = -2300, V_s = +325

s_0 (cm)	k_0	D (cm)	d/s_0	$[(k_0-3)/k_0]*(D/2s_0)$
0.4	24.89	88.11	3.38	96.86
0.45	22.23	83.85	3.00	80.60
0.5	20.11	80.29	2.70	68.31
0.55	18.37	77.25	2.45	58.76
0.6	16.93	74.63	2.25	51.17
0.65	15.70	72.33	2.08	45.01
0.7	14.65	70.31	1.93	39.94

Table III. 5 : Primary space focus investigation-- dependence of spectral characteristics on the extraction (repeller) and acceleration (flight tube) potentials of the CaO^+ peak from the 0.033% Eu:CaO sample.

ACCELERATION POTENTIAL -2100 Volts

Repeller Voltage (+V)	MEAN Resolution (FWHM in ns)	MEAN Intensity (mV)
400		
375		
350	125	0.60
325	85	0.60
300	78	0.50
275	78	0.63
250	68	0.67
225	52	0.93
200	57	1.10
175	88	0.90
150	82	0.67
125	90	0.60
100	115	0.43

ACCELERATION POTENTIAL -2200 Volts

Repeller Voltage (+V)	MEAN Resolution (FWHM in ns)	MEAN Intensity (mV)
400	70	0.50
375	67	0.55
350	62	0.70
325	62	0.83
300	49	1.13
275	57	1.40
250	63	1.40
225	68	1.10
200	98	1.03
175	95	1.00
150	88	0.80
125	110	0.80
100	120	0.60

ACCELERATION POTENTIAL -2300 Volts

Repeller Voltage (+V)	MEAN Resolution (FWHM in ns)	MEAN Intensity (mV)
400	59	1.37
375	58	1.50
350	58	1.80
325	58	1.83
300	60	1.83
275	78	1.73
250	100	1.50
225	108	1.50
200	125	1.23
175	168	1.00
150	200	0.97
125	213	0.87
100	225	0.70

ACCELERATION POTENTIAL -2400 Volts

Repeller Voltage (+V)	MEAN Resolution (FWHM in ns)	MEAN Intensity (mV)
400	68	1.93
375	63	2.00
350	70	2.10
325	82	1.97
300	92	1.87
275	112	1.77
250	132	1.57
225	162	1.50
200	188	1.60
175	213	1.40
150	302	1.13
125	343	0.83
100	508	0.70

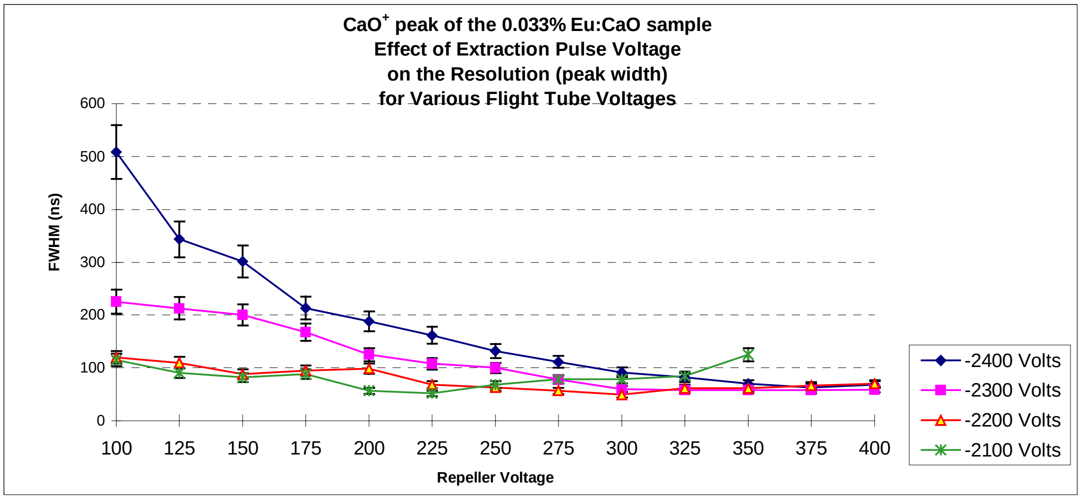

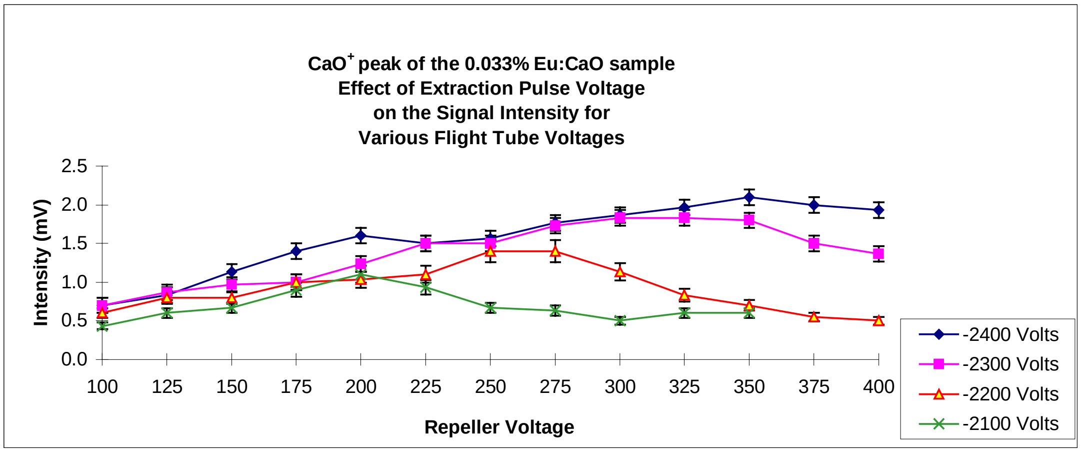

Figure III. 4: Primary space focus investigation-- dependence of spectral characteristics on the extraction (repeller) and acceleration (flight tube) potentials of the CaO^+ peak from the 0.033% Eu:CaO sample.

CaO^+ was used to gauge the FWHM and intensity dependence on the acceleration and extraction fields. The assumption was made that the shot-to-shot reproducibility of the CaO^+ yield was consistent for a given set of conditions. The characteristics of the CaO^+ peak, as Table III.5 and Figure III.4 reveal, show similar optimal conditions as the aluminum sample. Comparing the optimized E_d/E_s ratios for the Al^+ and CaO^+ samples (see Tables III.3(a) and (b)) confirms that the space focus is independent of the analyte.

III.3.2.-- Secondary space focus

After obtaining the first-order space focus by varying the extraction and acceleration fields, the reflectron voltages were likewise investigated to define the second-order focussing conditions. With our dual-stage reflectron instrument, both the front lens (-Voltage) and the rear lens (+Voltage) must be optimized to maximize the signal intensity and minimize the FWHM. After correcting for the initial spatial distributions of isomass ions through the primary space focus, initial kinetic energy distributions can be reduced by the reflectron to achieve the secondary space focus at the detector.

Analyzing the aluminum disk as before, 100 laser shots were averaged per spectrum, and ten spectra were averaged to obtain FWHM and intensity (peak height) data. The range of reflectron lens potentials chosen were those which were previously determined to generate appreciable ion yields. Using the optimized first-order space focussing conditions of E_d = -2300 Volts and E_s = +325 Volts, first the front lens potential was held constant at -920 Volts while the rear lens was varied. Similarly, the rear lens was later held constant (+340 Volts) while the front lens was varied.

As Table III.6 (a) and (b) and Figures III.5 and III.6 display, there is a narrow range of reflectron lens voltages (after the acceleration and repeller potentials are set) which will successfully reflect the ion packet to the detector to generate appreciable signal. This arises from signal intensity losses due to collisions with the reflecting lenses[46] and a broad ion packet from poorly chosen conditions.

It is clear that energy focusing (i.e. the secondary space focus) greatly enhances the resolution. Somewhat less influenced was the intensity of the signal, which might be attributed to the narrow conditions that generate any appreciable ion yield at all. The strict dependence of resolution on the proper choice of lens potentials highlights the importance of energy-focusing by the reflectron to narrow the ion packet.

The optimized electric fields which provide the highest quality mass spectra were ~+340 V and –940 V for the rear and front reflectron lenses, respectively. Such findings are vital for the characterization of the new time-of-flight instrument and confirmation of theoretical principles. Because a significant spectral improvement was achieved by

---

[46] D. Lubman, W. Bell, M. Kronick. *Anal. Chem.* **55** (1983) 1437.

Table III. 6 (a): Second-order space focus investigation--Optimization of the reflectron using the Al^+ peak of the aluminum sample-- Constant front lens potential.

Reflectron Voltages:		Signal Characteristics:	
rear lens (positive V)	front lens (negative V)	MEAN FWHM (ns)	MEAN Intensity (mV)
460	920	189	2.89
420	920	136	3.28
380	920	100	3.33
340	920	75	3.53
300	920	81	3.15
260	920	86	2.77
220	920	92	1.75

Table III. 6 (b): Second-order space focus investigation—Optimization of the reflectron using the Al^+ peak of the aluminum sample—Constant rear lens potential.

Reflectron Voltages:		Signal Characteristics:	
rear lens (positive V)	front lens (negative V)	MEAN FWHM (ns)	MEAN Intensity (mV)
340	1080	126	3.37
340	1040	107	3.28
340	1000	90	3.67
340	960	81	3.14
340	920	77	3.53

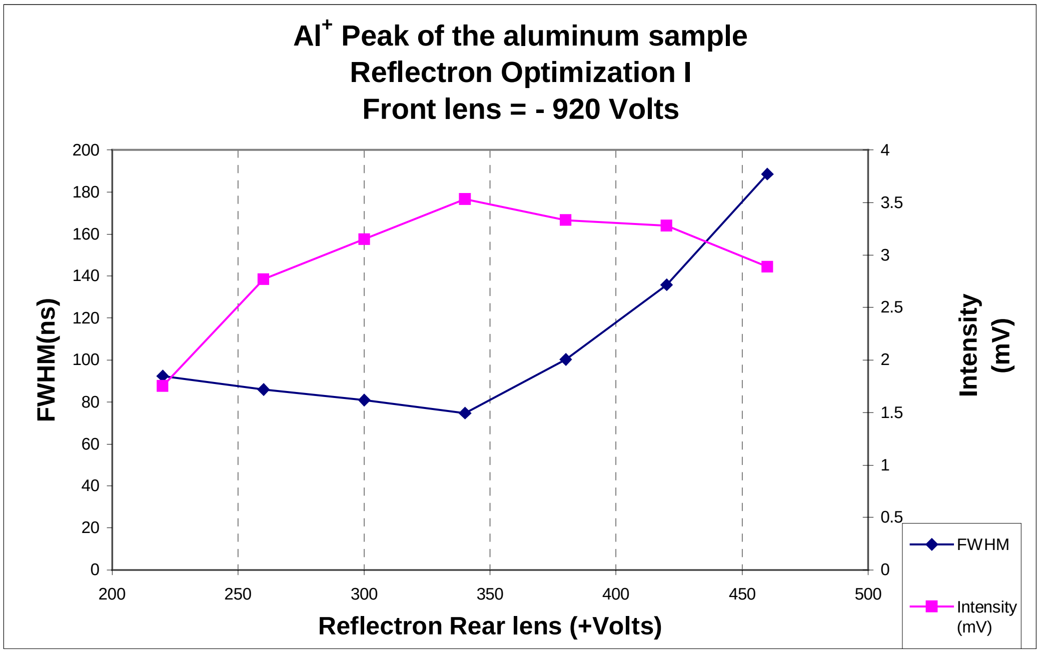

Figure III. 5 : Second-order space focus investigation-- Optimization of the reflectron-- Constant front lens potential.

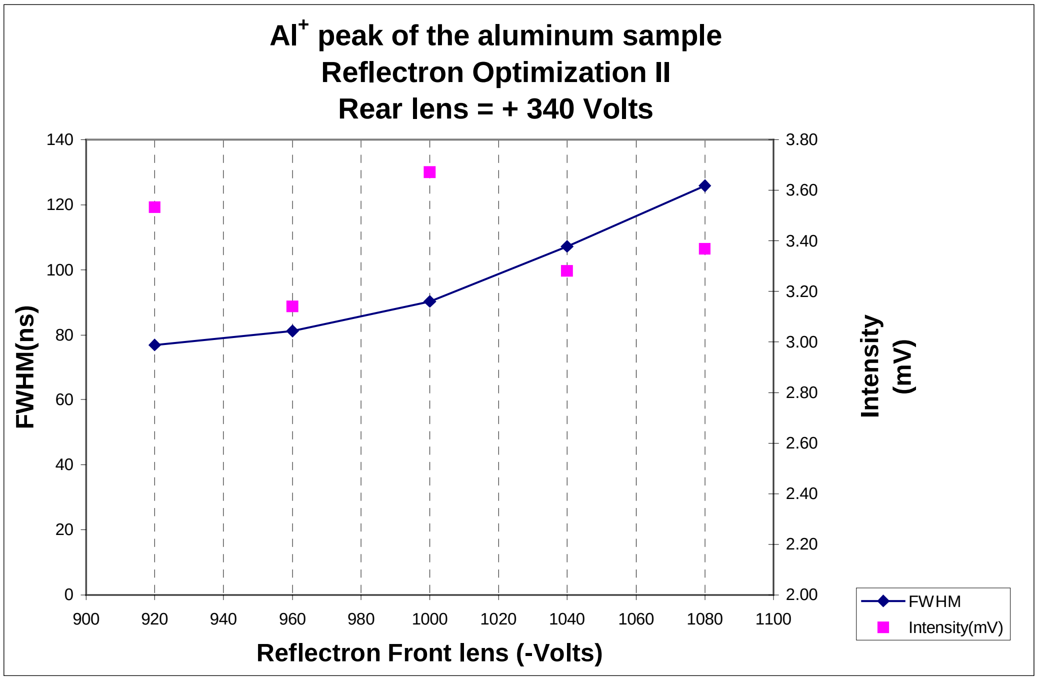

Figure III. 6 : Second-order space focus investigation-- Optimization of the reflectron-- Constant rear lens potential.

defining the space focus experimentally, future instrument operation is simplified; just refining the conditions for a given system is all that is subsequently required, rather than a complete re-optimization for each sample. Furthermore, the substantial increase in resolution that the energy-focussing reflectron provides reveals the significant initial kinetic energy distribution that our laser ionization system imparts.

III.4.-- RESOLUTION

Resolution with our LI-TOF-MS, as noted before, varies tremendously based on experimental conditions. Because of the limitations of linear mode, the discussion of experimentally achieved resolution will focus on the reflectron mode of operation. In addition to the reflectron, several subtle instrumental parameters impact the resolution as well. Data recording on the oscilloscope affects the resolution in several ways. Because of the fixed number of data points recorded by the oscilloscope, maximum oscilloscope resolution per ion peak can only be obtained if a limited mass range is recorded. The compromise in most spectra was made to display times-of-flight up to 100 μs simultaneously (masses up to about 500 amu). Such digitization problems had only a small impact on the spectra, but might limit the potential oscilloscope resolution. A more noteworthy factor is the mode of data collection, spectra compiled as an average of a number of laser shots, or “single shot” spectra were compared. Single-shot spectra provided narrow peak widths at the cost of a much lower S/N ratio. In addition, irreproducible metastable decay and adduct products which occur only for a few shots were observed, and ions randomly injected into the flight tube[47] lead to slightly more complicated spectra. By averaging several spectra (at least 20), peaks widths widened as resolution–limiting factors resulted in slightly different times of flight over the compilation period. The greater density of ions in the ionization source due to incomplete ion expulsion from previous pulses is possible, and large space-charge densities would compound as more laser shots are averaged. However, background noise was largely eliminated in the averaged spectra to produce a cleaner baseline, and peak identification was facilitated since the random ions diminish into the baseline. Higher S/N ratios can be achieved, as a comparison of Figures III.7 and III.8 shows.

---

[47] D. P. Myers, G. Li, P. Yang, G. M. Hieftje. *J. Am. Soc. Mass Spectrom.* **5** (1994) 1008.

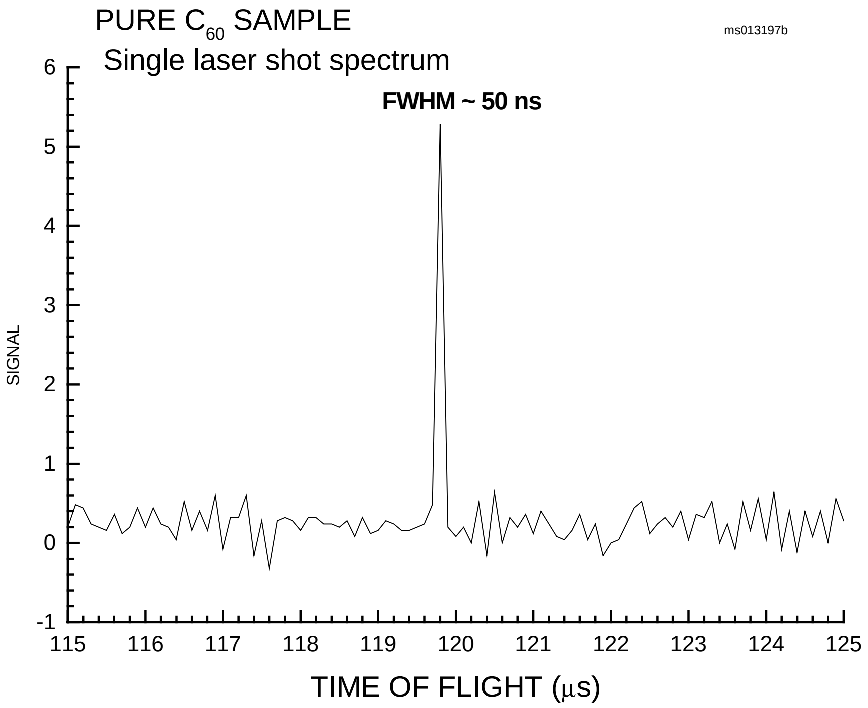

Figure III. 7 : Single-shot spectrum of pure C_{60}.

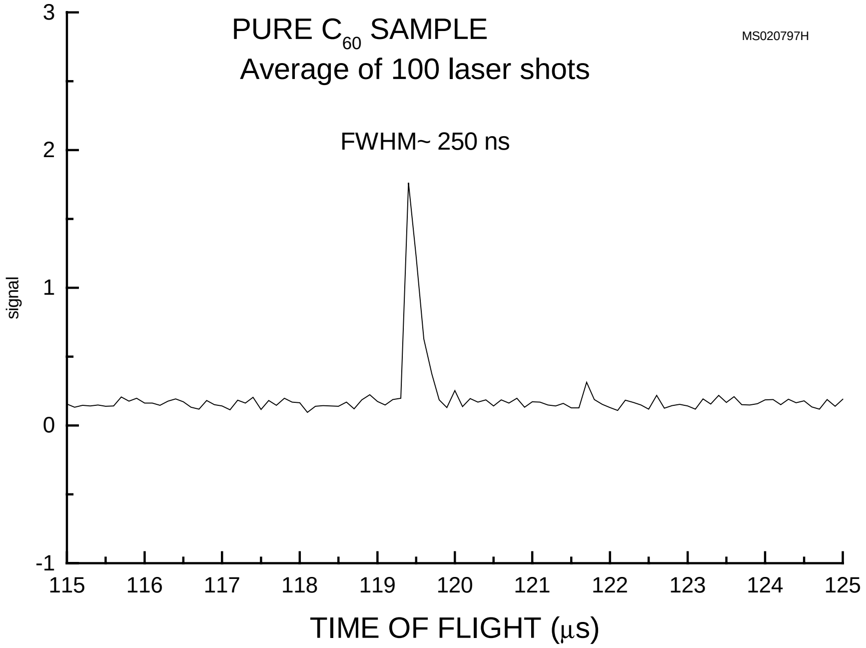

Figure III. 8 : Spectrum of pure C_{60} compiled as the average of 100 laser shots.

Several factors must be considered in determining the number of laser firings to be averaged. For metal foils and other samples that are thick, homogenous, and of high concentration throughout, averaging a large number of scans was possible. The laser ablation process removes only an insignificant amount of sample, and the signal is consistent. On the other hand, averaging a large number of shots on a different sample often provided poor results due to both the sample itself and the method of sample preparation. On a limited, thin film of sample (up to hundreds of microns thick), averaging many scans was impossible before the laser completely removed the sample to expose the probe surface. Since the sample removal caused by the ablation is relatively more significant, the signal deteriorated rapidly on these thin samples. This was most notable for the thinly deposited MALDI samples as will be discussed in chapter VI. Specific samples, even when deposited as thick films, were likewise found to provide better spectra when averaging fewer laser shots. Fullerenes in particular showed this problem, as a “fresh spot” had to be analyzed by rotating the sample probe per spectrum when over about 50 laser shots were averaged. This observation has been reported previously[48], and could be attributed to enhanced coupling of the laser energy with a fresh, unexposed surface. In addition, laser beam defocusing might occur as the depth of penetration changes the distance from the focal lens. This effect, though, is expected to be small due to the large focal distance of the lens that we employed.

Experimental resolution as defined by $t/2\Delta t_{FWHM}$ varied based on the masses of the analytes. Considerable broadening significantly increased all *averaged* spectra as mass increased. In single-shot spectra, FWHM’s on C_{60} were as low as 50 ns (see Figure III.7), whereas spectra averaged for 100 or more scans yielded peak widths in the 250 ns range (see Figure III.8). Resolutions, therefore, were about 1200, and 200, respectively, for the time-of-flight peak of approximately 120 μs.

For lower-mass ions, the averaging mode versus the single-shot mode of data acquisition affected the resolution less. For the aluminum disk samples, typical single-shot spectra displayed widths of 25 ns, while the peak widths of spectra averaged for up 100 laser shots generally remained under 50 ns. For the Al^+ time-of-flight of 23 μs, resolution thus calculates to 460 and 230, respectively. Similar peak widths were obtained for surface impurities such as sodium (21 μs time-of-flight) and potassium (28 μs time-of-flight), to yield comparable resolution values. Indium (113 amu) spectra displayed slightly wider peaks for averaged spectra (25 laser shots), but the time-of-flight was double that of aluminum, for calculated resolution values slightly over 400. For other samples such as the doped metal oxides, similar results were obtained.

Several explanations could account for the wide peak widths of the high-mass fullerene ions. Most notable is the experimental configuration of our ionization chamber, as the analyte must rise from the sample surface to the flight tube axis (about 4.2 cm). The longer extraction pulse delay time that is required for high-mass species to travel this distance provides ample broadening possibilities because several factors become prominent for longer times in the ionization region. Coulombic repulsions become more significant due to the high charge density generated in the laser-induced plasma[43] and large size of the fullerene cage. Over a longer period of time, such affects compound and lead to a range of flight tube entrance times. Also, the turn-around-time problem is expected to have more of an impact as the spread between the ions has more time to widen. In addition, kinetic energy distributions may not be adequately corrected for in the reflectron. Penetration into the reflectron would be low for these high-mass, low-velocity species, and thus the smaller path difference might not have achieved optimal second-order focusing. A final aspect is the general broadening as a function of the time spent in the spectrometer. This broadening is not uncommon because the lower velocities of the ions could increase collisional effects. The resolution equation largely portrays this, balancing the peak width increase by the longer time of flight to hopefully provide similar resolution values.

The definition of resolution = $t/2\Delta t_{FWHM}$ could be a bit misleading. Adequate resolution was clearly achieved in the low-mass range, but the calculated resolution underscores this point due to the low time-of-flight, t, in the numerator. With our instrument and digitization settings, it appears that optimized single-shot peak widths (Δt_{FWHM}) minimize in the 20 ns range for all times of flight below about 40 μs. Thus, the

---

[48] E. Cromwell, P. Arrowsmith. *Anal. Chem.* **67** (1995) 131.

maximum resolution possible according to the relation $t/2\Delta t_{FWHM}$ can only be 625 for ions of 25 μs time-of-flight. Depending on the rate of broadening as a function of time, the calculated values could skew the resolution assessment.

III.5.-- MASS CALIBRATION

Mass calibration for elemental samples such as the pure metal foils was straightforward, since the main ion provided the only appreciable signal and isotope analysis confirmed the peak assignment. In addition, surface impurities such as Na^+ and K^+ could be identified by using the approximation:

$$\frac{\sqrt{m_1}}{\sqrt{m_2}} = \frac{t_1}{t_2}$$

Equation III. 1: Approximate mass calibration.

where m_1 and m_2 are the masses of the known and unknown ions, respectively, and t_1 and t_2 are their corresponding times-of-flight.

Over a limited mass range, this approximation allowed the identification of other species present.

A similar procedure as with metal foils allowed mass determination for the more complicated doped metal oxide systems. In the case of 0.033% Eu:CaO, for example, two abundant signals occurred for m/z values of approximately 40 and 56 amu. Based on their separation by 16 amu and the isotopic distribution of Ca^+, they were identified as Ca^+ and CaO^+.

Once two masses and their corresponding times-of-flight were known, a calibration line was plotted according to

$$\sqrt{m} = at + b$$

Equation III. 2: Experimental mass calibration line equation.

where m is the mass of the known species, t is the corresponding time-of-flight, and a and b are calibration constants. After graphing and best-fit lines were drawn, other ion peaks were confidently identified.

The more complicated spectra of the high-molecular weight inorganic samples were calibrated in a different manner. Spectra of the aluminum sample disk that held the sample provided one data point of the calibration line in the low-mass region. To generate a second point at a higher mass, a C_{70} sample was placed on the same sample plate as the analyte. By rotating the sample probe slightly to this C_{70} sample, the prominent ions peaks corresponding to C_{60} and C_{70} were generated and used for a total of three (Al^+, C_{60}^+, C_{70}^+) data points. Again, a best-fit line provided the necessary method of identification of analyte peaks through this wide mass range. For matrix-assisted samples, the main matrix ion peak often provided an additional data point. From prior analyses of the matrix by itself, the matrix molecular ion or most prominent species [i.e. $(\text{matrix} - OH)^+$] was identified. Upon ablation of the inorganic analyte, this matrix peak was again identified and used for internal calibration.

Excellent calibration results were obtained in both range and accuracy. As an example, Figure III.9 shows a typical calibration line and the resulting mass values. Regression values in nearly all cases were unity, and mass accuracies were good to at least one amu through 1000 amu, with accomplishments even greater in the region under 200 amu. Taking the $^{39}K^+$ peak, for instance, a calculated mass difference from the expected 38.96 amu is only 0.02 amu for better than 99.95% accuracy. For higher masses, Figure III.9 reveals that the experimental mass of the C_{50}^+ peak, 600.12 amu, differs from the known mass, 600.55 amu, by only 0.072%. One slight problem when using C_{60}^+ as a reference, however, might arise because resolution limitations of the spectra could not distinguish masses 720 and 721 amu; the centroid of the peak was assumed to correspond to the isotope-factored mass of 720.66 amu (60 atoms x 12.011 amu/atom). Mass ranges could be extrapolated to generate values even for the large molecular clusters formed from ablation of the fullerenes, as again shown in Figure III.9, and were better than 0.1% accurate for the $C_{180}^+$and C_{274}^+ species. Extending too far beyond the calibration points, of course, results in less accurate absolute mass

Calibration species	Mass (amu)	Time of flight (microseconds)	sq. rt. of mass
Al	26.98	23.27	5.1942
C_{60}	720.66	119.55	26.8451
^{102}Ru	102	45.03	10.0995

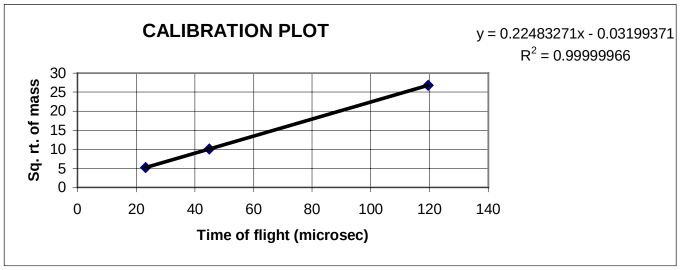

CALIBRATION EQUATION: $Mass^{1/2} = 0.22483271 * tof - 0.03199371$

Expt. tof (microsec)	Calculated sq. rt. of mass	Mass (expt.)	Carbon # (expt.)	Carbon # (known)	Mass (known)	% difference in mass
21.46	4.7929	22.97	(sodium)	--	22.99	0.078
27.91	6.2431	38.98	(potassium-39)	--	38.96	0.041
28.63	6.4050	41.02	(potassium-41)	--	40.96	0.155
109.1	24.4973	600.12	49.96	50	600.55	0.072
111.3	24.9919	624.59	52.00	52	624.57	0.004
113.4	25.4640	648.42	53.99	54	648.59	0.027
115.5	25.9362	672.69	56.01	56	672.62	0.010
117.5	26.3858	696.21	57.96	58	696.64	0.061
119.5	26.8355	720.14	59.96	60	720.66	0.071
119.6	26.8580	721.35	60.06	60	720.66	0.096
129.1	28.9939	840.65	69.99	70	840.77	0.015
146.5	32.9060	1082.80	90.15	90	1080.99	0.168
147.9	33.2208	1103.62	91.88	92	1105.01	0.126
149.4	33.5580	1126.14	93.76	94	1129.03	0.256
151.0	33.9177	1150.41	95.78	96	1153.06	0.229
152.7	34.3000	1176.49	97.95	98	1177.08	0.050
155.8	34.9969	1224.79	101.97	102	1225.12	0.027
157.2	35.3117	1246.92	103.81	104	1249.14	0.178
161.7	36.3235	1319.39	109.85	110	1321.21	0.137
163.1	36.6382	1342.36	111.76	112	1345.23	0.214
167.4	37.6050	1414.14	117.74	118	1417.30	0.223
168.9	37.9423	1439.61	119.86	120	1441.32	0.118
170.3	38.2570	1463.60	121.85	122	1465.34	0.119
202.2	45.4292	2063.81	171.83	172	2065.89	0.101
206.9	46.4859	2160.94	179.91	180	2161.98	0.048
255.2	57.3453	3288.49	273.79	274	3291.01	0.077

MEAN % DIFFERENCE IN MASS 0.104

Figure III. 9 : Calibration example and mass accuracies.

determinations, and ions of very high mass tend to have times-of-flight which are slightly shorter than expected[49].

III.6.-- ION YIELDS FOLLOWING LASER ABLATION

III.6.1.-- Reproducibility

III.6.1.1-- Reproducibility of ion yields from a homogeneous sample

To gauge the reproducibility of our laser ablation process and ion transmission through the spectrometer, an Al plate was sampled (5/8-inch diameter, 1/8-inch thick). The peak intensity (height), as measured directly from the oscilloscope, and the peak area, as calculated by integration, were generated for a range of laser energies. To avoid excessive hole-digging and beam defocusing, a fresh aluminum spot was ablated for each laser energy. Laser ablation was performed for a variety of laser energies, and a 25-cm focal length lens created an approximate spot radius on the sample target of 11μm. The first spectrum generally produced some amounts of surface impurities such as sodium and potassium ions, so this data was discarded. One-hundred laser shots were again averaged per spectrum, and ten spectra were then averaged to generate the mean peak intensity and area data as shown in Table 7.

Table III. 7: Ion yields following Al^+ ablation.

LASER ENERGY (μJ)	**DETECTOR VOLTAGE (-V)**	**Al^+ Height (mV) Mean**	**%RSD**	**Al^+ Area (mV x μs) Mean**	**%RSD**
12	1700	1.42	23.79	0.0993	17.34
17	1700	1.88	12.99	0.1225	15.73
19	1700	2.34	18.06	0.1888	18.80
19	1525	1.21	23.10	0.0948	19.67
25	1525	3.05	20.52	0.3207	17.71
25	1200	1.22	18.64	0.0798	12.33
45	1100	1.18	6.83	0.1214	9.73

---

[49] R. Cotter. *Anal. Chem.* **64** (1992) 1027A.

Referring to Table III.7, there is a high relative standard deviation among both the area and peak height yields. Several laser energies were used, ranging from 12 to 45 μJ, and the %RSD data for peak area when using laser energies under 45 μJ is 14% to 19%, which is comparable to other work[50,51,52]. For peak height data of the same laser energies, deviations are in most cases higher, by about 125%. The precision of ion yields improved greatly when using a high laser energy (45 μJ). Both the height and area data show improvements in reproducibility by about 250% and 75%, respectively, from the other energies investigated. Further laser energy increases were prohibited due to detector saturation for all gain settings.

Some important conclusions can be drawn from the reproducibility data. Primarily, absolute quantitation based solely on the peak area or height yielded high standard deviations for all laser energies used. The complex laser-material interactions produce a distribution of yields for even a simple system such as the homogeneous aluminum sample. Since some improvements were seen with high energies, it is apparent that the number of ions generated by laser ablation is highly affected by the stabilization of the laser itself. It seems likely that laser jitter impacts lower laser energies in a larger proportion compared to higher laser energies. With estimates of the reproducibility of laser output energy of 2-10%[51], up to 10% of the experimental %RSD might be attributed to laser fluctuations.

As noted earlier, the area under the peak is a direct indication of the number of ions produced. The peak height, though, appears a rapid, useful estimate. In fact, a noted anomaly should be highlighted looking at the data for a laser energy of 17 μJ as the peak height reproducibility (12.99 %RSD) is better than the peak area (15.73 %RSD). This

---

[50] R. Mansoori, M. Johnston, A. Wexler. *Anal. Chem.* **66** (1994) 3681.

[51] K. Dittrich, R. Wennrich. Chap. 5, in J. Sneddon, Ed. S*ample Introduction in Atomic Spectroscopy.* New York: Elsevier, 1990.

[52] D. Cremers, L. Radziemski. Chap. 5 in L. Radziemski, R. Solarz, J. Pairsner, Eds. *Laser Spectroscopy and Its Applications.* New York: Marcel Dekker, 1987.

likely arises from a wider distribution in the broadness of the peak, which affects the area measurement but not the height assessment.

III.6.1.2-- Reproducibility of ion yields in a heterogeneous sample

A similar investigation was performed on a more complex sample, a 2-mm thick 0.033% Eu:CaO pellet. By comparing the reproducibility for the homogenous aluminum system with the heterogeneous doped metal oxide, it might be possible to assess some of the causes for the variation in ion yields. The two most abundant ions, $^{40}Ca^+$ and $^{40}Ca^{16}O^+$, were gauged over three laser energies, 18 μJ, 22 μJ, and 25μJ (detector gains are different for each). Data was compiled as with Al^+, and is displayed in Table III.8.

Table III. 8 : Ion yields following laser ablation.

LASER ENERGY (μJ)	**Ca^+ Height (mV)**		**Ca^+ Area (mV x μs)**		**CaO^+ Height (mV)**		**CaO^+ Area (mV x μs)**	
	Mean	**%RSD**	**Mean**	**%RSD**	**Mean**	**%RSD**	**Mean**	**%RSD**
18	1.23	20.06	0.233	14.89	1.05	19.20	0.0831	15.58
22	2.86	16.16	0.490	18.67	0.92	12.98	0.0506	14.62
25	3.83	11.96	0.776	14.51	1.01	19.55	0.0542	16.99

As was observed with the aluminum sample, the peak height and peak area %RSD values of both the Ca^+ and CaO^+ yields are approximately 10-20% for all of the laser energies used. It seems that this reproducibility range could be the goal of studies with our instrument and ionization method. Again, laser instability highly affects the variations of the ion yield. Furthermore, the other factors governing the ion yield, such as preferential ablation, heat dissipation in the sample, and matrix effects, are increasingly significant in the more complex doped metal oxide system when compared to the aluminum sample. However, since the reproducibility data in the homogeneous aluminum and in the more complex doped metal oxide are comparable over these laser energies, it seems that laser instabilities are highly responsible for the variations observed. This again highlights a major problem in absolute quantitation following laser ablation.

III.6.1.3-- Improving the reproducibility through a ratio technique of two peaks

As a potential solution to such problems in the absolute reproducibility of a single ion, a ratio technique was explored using the Ca^+ and CaO^+ yields. Such a study addresses the effects of laser energy fluctuations and instrumental variation, as both peaks should be affected in the same manner. It is important to note that the instrumental parameters, most notably the extraction pulse delay time, were held constant throughout the investigation due to the yield dependence on extraction pulse delay. The repeller delay chosen was approximately the average of the optimum for each mass.

Referring to Table 9, the precision of the relative intensity ratio (Ca^+/CaO^+) is indeed improved over the individual precisions. Most notable are the strides made in peak area reproducibilities, which improved by 130%, 174%, and 294% for laser energies of 18 μJ, 22 μJ, and 25 μJ, respectively. It is curious that peak heights did not offer greater reproducibility through ratioing, and in fact are slightly worse for the data of 22 μJ and 25 μJ. Overall, the improvements support the need for a reference peak or internal standard when addressing reproducibility in ion yields. Concentrating on relative data decreases variations.

The possible dependence of bare element and oxide production as a function of laser fluctuations may complicate the use of Ca^+ and CaO^+ peaks in the ratio technique. As will be discussed in Chapter IV, there is a complex dependence of Ca^+ and CaO^+ yields on laser energy, and thus the ratios of the two species may not fully correct for laser instabilities. Nonetheless, significant improvements especially in peak area precision were achieved through the ratio technique.

Table III. 9: Reproducibility improvements by the ratio technique.

LASER ENERGY (μJ)	**%RSD Ca^+**		**%RSD CaO^+**		**%RSD of ratio Ca^+/CaO^+**		**Mean Improvement**	
	height	**area**	**height**	**area**	**height**	**area**	**height**	**area**
18	20.06	14.89	19.20	15.58	5.77	11.70	340%	130%
22	16.16	18.67	12.98	14.62	17.57	9.57	-121%	174%
25	11.96	14.51	19.55	16.99	17.34	5.41	-110%	294%

III.6.2.-- Number of ions detected

From the peak area data obtained after integration, the ion yield from ablation of the Al^+ samples was approximated. Using the data for a laser energy of 45 μJ with the aluminum sample, Equation I.1 from Chapter I quantitates the actual number of Al^+ ions experimentally detected based on the current output of the multichannel plate. Assuming a detector gain of about 5×10^4, the number of ions detected is approximately 15,000.

A beam size measurement made at the position of the lens generates an approximate laser spot radius of 11 μm for our laser on the sample surface (focal point) according to the Gaussian spot size equation (See Equation II.1 of chapter II). The 45 μJ laser energy at the lens thus translates to an actual laser fluence of ~0.112 $\mu J/\mu m^2$ on the sample surface. Taking the atomic radius of aluminum or 0.143 nm, a calculation reveals that about 6.24×10^9 atoms will actually be struck by the laser spot per monolayer of sample.

The overall efficiency, defined as the number of ions detected to the number of atoms struck by the laser, is therefore roughly only 2.43×10^{-4} %. This assumes that all atoms of only the first monolayer are ionized, which is not a true picture of the ionization process, as ions are produced from subsurface layers, especially in the centroid of the beam spot. In addition, not all of the atoms struck in the monolayer will be removed from the surface and ionized. However, with this approximation as the basis, the overall efficiency can be broken down into losses from many sources. Laser-material interactions such as desorption and ionization efficiencies (positive ions formed per atoms removed from surface) are difficult to quantitate, but estimates of about 1% are common[53], with some estimates as low as 0.1% to 0.01% for MALDI techniques[54]. Other losses that are typical for all TOF instruments involve ion neutralizations from collisions between ions in the extraction process or the flight tube, and neutralizations as ions strike the electric field grids (90% transmission for Ni mesh). Common for

---

[53] N. Nogar, R. Estler. Chap. 3, in D. Lubman, Ed. *Lasers and Mass Spectrometry*. New York: Oxford University Press, 1990.

[54] P. Voumard, Q. Zhan, R. Zenobi. *Rev. Sci. Instrum.* **64** (1993) 2215.

multichannel plate detectors like ours is an efficiency of approximately 45%[55]. Also, transmission has been especially problematic through reflectron instruments[46].

A particular problem in our instrument is the significant ion yield dependence on the extraction pulse delay time due to the sample-to-flight tube axis travel path. As is discussed in Section III.7, optimization for each mass is vital. Even after optimization, however, the absolute transmission of ions from the sample into the flight tube will be compromised in the rise distance from the sample surface to the flight tube axis. Since material leaves the surface in a range of directions, the charged species may strike the acceleration or ground plates in the source chamber. Also, ion-ion neutralizations from collisions are increased due to the longer time in the ionization region, and cooling above the sample surface leads to atom formation from initially-produced ions[56].

Table III. 10: Transmission estimates in our LI-TOF-MS.

Approximate Transmission	**Explanation of Ion Loss**	**Basis for Estimate**
0.1%	Laser ablation process (removal of species from sample and ionization)	Literature
81%	Collisions with the 2 Ni grids in the TOF-MS (90% efficiency each)	Instrument specifications
45%	Detector efficiency	Instrument specifications
90%	Collisions of ions with flight tube walls	Personal estimate
75%	Reflectron efficiency- ions entering secondary flight tube successfully	Personal estimate
25%	Extraction efficiency- ions removed from sample entering the flight tube	Personal estimate
6.15×10^{-3}%	**TOTAL EFFICIENCY**	

---

[55] Microchannel Plate Detector Manual. Comstock, Inc.

[56] W. Sdorra, K. Niemax. *Spectrochim. Acta.* **45B** (1990) 917.

For a general estimate of transmission from each step of our LI-TOF-MS process, Table III.10 accounts for the low efficiency (2.43×10^{-4} %) observed. The estimates reveal an expected efficiency of ~ 6.15×10^{-3}%, with some flexibility for personal estimates and the particular conditions of our LI-TOF-MS. In particular, the 25% successful extraction of the ablated ions may be a bit hopeful.

III.7.-- ION VELOCITIES FOLLOWING LASER ABLATION

Our instrumental configuration enables the analysis of some fundamental processes that occur during laser ablation. The adjustable time delay between the laser firing and the extraction pulse propelling these ions out of the ionization region (0.1 to 100 μsec) allows the ablated ions to rise to the flight tube axis. After "scouting" various delay times (1 μs to 80 μs), refinements in the extraction delay time were required to obtain the best signal for each particular ion. Correlating the optimal delay time for various ions offers insight into the relation between the ion mass and its ablation velocity.

III.7.1.-- Optimum delay time and velocity dependence on the analyte mass

Since different ions travel to the flight tube axis in different amounts of time, the optimum delay varied with the species investigated, as is shown in Table III.11.

Plotting this optimum delay versus the ion mass in Figure III.10 reveals a square root dependence. The trendline, depicting the dependence of optimum delay on mass to the 1/2 power, serves as a useful guide for the expected delay time should different analytes be studied.

A more fundamental analysis of the laser ablation process relates the optimum delay time to the velocities of the removed ions. Because the surface-to-flight-axis distance is 4.2 cm in our instrument, the velocity of an ion following ablation is obtained by dividing this distance by the time of travel. Referring again to Table III.11, there is a steady decrease in the ejection velocity as the mass of the detected ion increases; for example, the velocity of the Al^+ ion as it rises from the sample surface is an order of magnitude greater than the fullerene (C_{120}^+ and C_{180}^+) clusters.

A clearer representation how the ablation velocity depends on mass is shown graphically in Figure III.11. A rather smooth trend is observed with a square root falloff, which leads to deductions about the kinetic energies of the ablated material. As

Table III. 11: Optimum extraction pulse delay times and the corresponding velocities and kinetic energies of ablated ions.

Species	Mass	Optimum delay	Velocity	Kinetic energy	
(major isotope)	(amu)	(microseconds)	(m/s)	(Joules)	(eV)
O	16	4.8	8723	1.01E-18	6.32
Al	27	7.2	6143	8.46E-19	5.29
Ca	40	9.7	4316	6.18E-19	3.86
CaO	56	10.2	4100	7.81E-19	4.88
Y	89	10.2	4100	1.24E-18	7.76
YO	105	12.3	3417	1.02E-18	6.36
In	113	12.3	3583	1.20E-18	7.53
Eu	151	17.4	2412	7.29E-19	4.56
EuO	167	21.5	1952	5.28E-19	3.30
W	182	22.0	2000	6.04E-19	3.78
C_{60}	720	45.1	932	5.19E-19	3.24
C_{70}	840	45.1	932	6.05E-19	3.78
C_{120} cluster	1440	67.6	621	4.61E-19	2.88
C_{180} clusters	1960	67.6	621	6.28E-19	3.92
		MEAN KINETIC ENERGY		7.71E-19	4.82
		Standard Deviation		2.56E-19	1.60

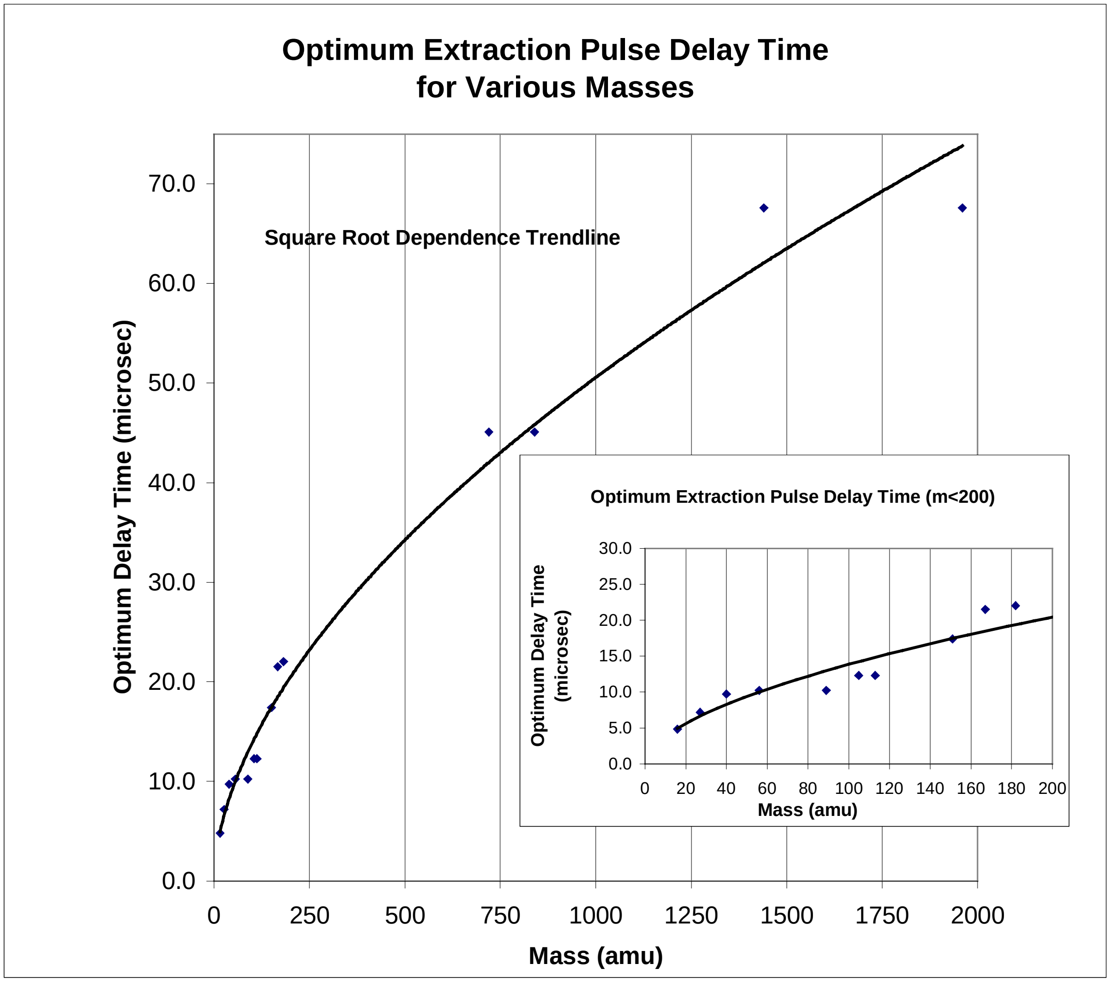

Figure III. 10: Plot of the optimum repeller pulse delay time as a function of the mass of the ablated ion.

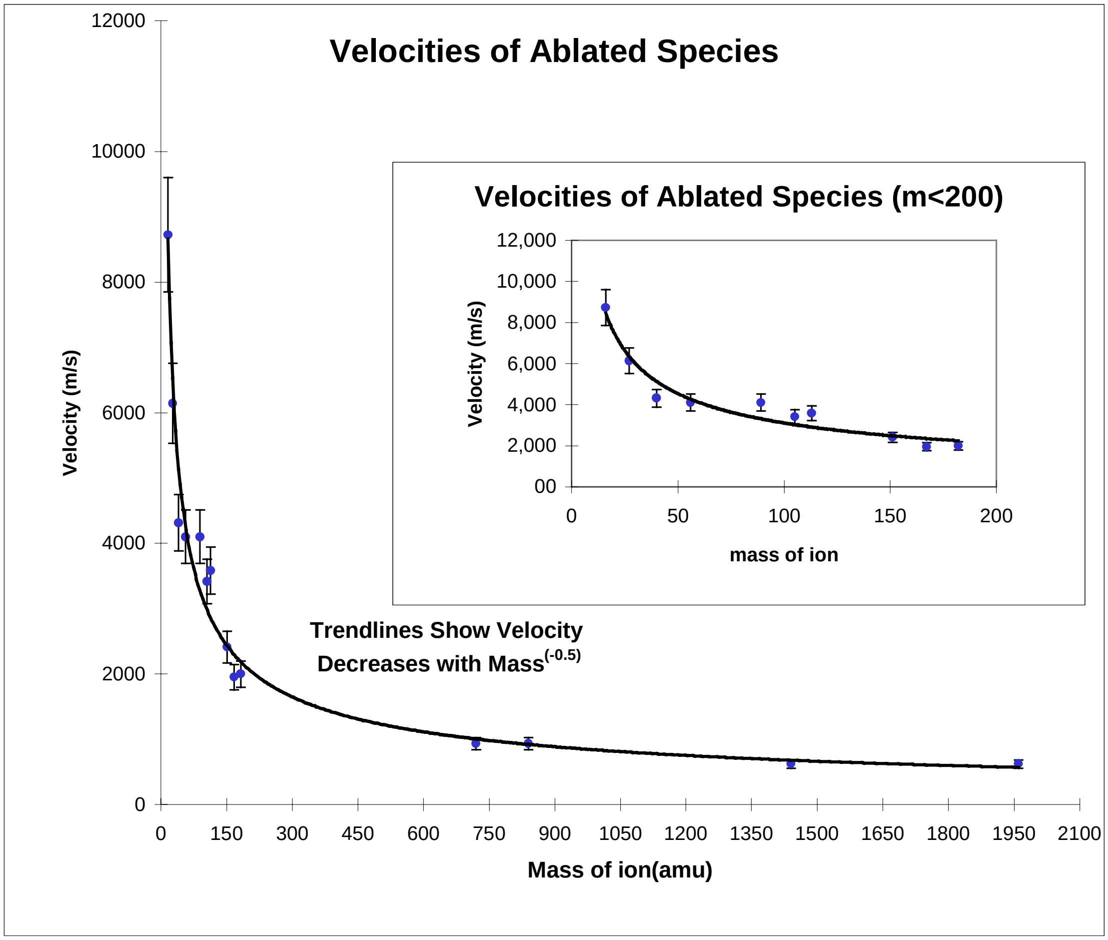

Figure III. 11: Velocities of the ablated ions as a function of mass.

Table III.11 shows, the kinetic energies for all the ablated species that were studied (with masses from 16 to 1960 amu) are within a factor of three difference from the lowest to the highest. This demonstrates that the kinetic energies of the ablated species are largely independent of mass. Because the velocity data fits well to the trendline of mass to the -1/2 power, the constancy of kinetic energies is confirmed, since mass, kinetic energy, and velocity are related through:

$$KE = \frac{1}{2} \times mv^2$$
$$v = \sqrt{\frac{2 \times KE}{m}}$$

Equation III. 3 (a) and (b): Velocity of ablation related to the kinetic energy of the ablated ion.

where m and v are the mass and velocity of the particle, respectively, and KE is its kinetic energy following ablation.

The conclusion to be drawn, therefore, is that the energy imparted to the ion from the laser pulse (10 to 50 μJ pulse energies were studied) is rather independent of the species. One way to analyze this finding is to look at the ablation process as a collisional interaction, where the laser beam strikes the material and removes species from the surface. The actual striking procedure imparts equal energy to the ions regardless of the target identity. The characterized analytes (except for the fullerenes), it should be noted, do not have strong absorptions in the 355-nm range of our Nd^{3+}:YAG ablation laser. Also, the ionization potential of each of the analytes is well below the laser energy.

III.7.2.-- Minimum and maximum ablation velocities

For each particular species, a “window” of usable delay times was experimentally determined. Although Table III.11 shows the optimum delay time, the ion packet, which forms from the laser pulse, does generate a less intense but detectable signal within a range of microseconds from the optimum delay. Table III.12 lists the repeller delay ranges for Al^+, Eu^+, and C_{60}^+, and the corresponding velocity and energy ranges follow in Table III.13:

Table III. 12: Window of successful extraction delay times for Al^+, Eu^+, C_{60}^+.

SPECIES	**Minimum delay (μs)**	**Optimum delay (μs)**	**Maximum delay (μs)**
Al^+	4.6	7.2	11.3
Eu^+	11.7	21.5	29.3
C_{60}^+	34.2	45.1	70.3

Table III. 13: Range of velocities (orthogonal ejection) based on the window of successful extration pulse delay times.

SPECIES	**Velocity Range (m/s)**	**Energy x 10^{-19}(Joules)**
Al^+	3712 to 9130	3.09 to 18.6 (1.93 to 11.6 eV)
Eu^+	1433 to 3589	2.57 to 16.1 (1.61 to 10.08 eV)
C_{60}^+	597 to 1228	2.13 to 9.01 (1.33 to 5.63 eV)

Several factors may explain this "window" of extraction times that generate ion signals. In addition to the natural variation of kinetic energies of the ablated material, various angles of ion ablation, which have been noted to be up to 30°[57], will yield different velocity components of the species in the relevant (z) direction. Also, the flight tube diameter (2 cm) must be considered. Although the 4.2 cm represents the center of the flight tube, 5.2 cm to 3.2 cm comprise the upper and lower openings, respectively. Each of these possibilities will be evaluated later.

To simplify the discussion of the delay range windows, the energy of repeat laser pulses will be assumed constant, and only the orthogonal situation (0°) will be addressed. For the mean Al^+ velocity, the ion packet rises to 2.83 cm for the minimum delay time for which signal was detected. Since it is unlikely that ions rising to only 2.83 cm would enter the flight tube, we can conclude that a few ions do receive more kinetic energy than

---

[57] S. Alimpiev, M. Belov, S. Nikiforov. *Anal. Chem.* **65** (1993) 3194.

the majority. Although operating at this extreme produces only trace ion yields, it may serve as some guide to the variation in velocities and kinetic energies which are possible for a few of the ions of the same species to acquire as they are emitted from the surface. The maximum velocity, approximated when the trace Al^+ ions travel the 4.2 cm height in 4.6 microseconds, is 9130 m/s (148% of the mean Al^+ velocity) and relates to a kinetic energy upper limit of 1.87×10^{-18} joules (11.69 eV). Similar calculations for Eu^+ yield a maximum velocity of 3589 m/s (150% of the velocity of most ions) and thus a kinetic energy of 1.61×10^{-18} joules (10.06 eV). Likewise, the C_{60}^+ maximum velocity is 1228 m/s (132% of the velocity of most ions) and places a maximum kinetic energy at 8.96×10^{-19} joules (5.60 eV).

Minimum energies of the ions following ablation are more difficult to ascertain from experimental data, since the angular dependence will decrease the effective velocity (that is, the z-component of the velocity). Again, only the orthogonal case will be considered and the laser energy assumed constant. The minimum velocity of Al^+, Eu^+, and C_{60}^+ ions would occur for the maximum delay times of 11.3, 29.3, and 70.3 microseconds, respectively. Calculating the velocity of the slowest Al^+ ions reveals a value of 3712 m/s (60.4% of the mean) and an energy of 3.15×10^{-19} joules (1.97 eV). Identically, Eu^+ minimum velocities could be bracketed at 1433 m/s (59.4% of the majority), relating to 2.66×10^{-19} joules (1.66 eV) of kinetic energy. The lower velocity limit for C_{60}^+ would fall at 597 m/s (64% of the mean), giving a kinetic energy of 2.16×10^{-19} joules (1.35 eV).

Referring again to Table III.13, a few observations need special explanation. The interesting finding that the maximum velocity of C_{60}^+ is only 132% of the majority while the maximum velocities of Al^+ and Eu^+ are about 150% of the major ion packet is a bit problematic to explain. One possibility is that the much larger C_{60}^+ is less likely to have trace ions reach the flight tube axis at apparently higher velocities due to space-charge effects, since C_{60}^+ is less prone to velocity changes after collisions due to its low charge-to-mass ratio.

III.7.3.-- Angular dependence

Ablation and ejection of particles from a surface naturally occur at a variety of angles, and calculations were made for three representative angles (10°, 20°, and 30° from the normal) for the mean velocities of the three ions. The z-component of the total velocity, as given by the cosine of the angle from the normal, governs the time required to reach the flight tube axis. For the calculated angular range, the decrease in the height of Al^+ ions for the optimum delay time is 0.54 cm, while for the maximum delay time it is 0.93 cm. This is one possible reason for signal generation at longer than optimum delay times and would lead to apparently slower velocities.

The angular dependence is especially noticeable in the case of C_{60}^+, which has an upper bound of extraction delay times of 70.3 microseconds. This finding is a full 156% longer than the ideal extraction time. For the 30^o case, the average height of the ion packet would be approximately 5.67 cm at this maximum delay since the perpendicular velocity is only 807 m/s. Therefore, it is quite possible that some stray ions ablated at this angle could linger near the flight tube axis long enough to be projected into the flight tube even by the highly delayed pulse. Again, this is reflected in an apparently slower velocity of ablation. The velocity dependence on ejection angle is highlighted in Table III.14.

Table III. 14: Velocity dependence on angle of ion ablation.

SPECIES	**Vertical Velocity (m/s) following emission at**			
	0°	**10°**	**20°**	**30°**
Al^+	6143	6051	5773	5320
Eu^+	2412	2376	2267	2089
C_{60}^+	932	918	876	807

There are numerous complications when attempting to bracket a “minimum” and “maximum” velocity of ablated species from the sample surface. Primarily, the angular dependence is vital to the vertical height that is traveled in a given amount of time. With the exact angle of emission unknown, Table III.14 shows that the vertical velocity can decrease by up to 87% for ions traveling from the surface at 30°. Furthermore, the ease of ablation of some ions must be considered. Random ions emitted from the surface due to successive heatings of the sample will spontaneously enter the flight tube at different times from the majority of the ions. Other atoms are held with decreased strength to the surface in different matrices and may leave the sample with increased energy due to a decrease in binding energy. Furthermore, space-charge effects, where nearby positive ions cause repulsions, also change the velocity of the ions. In addition, fluctuations in the power density of the laser beam arising from instability in the laser itself and deviations from the ideal focal point also might cause a range of energies to be imparted to the ablated ions.

III.7.4.-- Flight tube diameter considerations

One other significant complication is that the 4.2-cm flight tube axis-to-sample surface represents the center of the flight tube; the heights of successful entrance into the flight tube certainly are not limited to the ideal 4.2-cm distance. In fact, the instrument has a circular entrance region that is approximately 2 cm in diameter. Thus, distances from 3.2 to 5.2 cm form the minimum and maximum perpendicular heights for the bottom and top of the circular openings, respectively. If such ranges of possible entrance heights allow ions to enter the flight tube at these various distances, the true velocity spread could be narrowed considerably. Referring to Table III.15, the minimum and maximum heights attained for the orthogonal case are rather close to these distances for the mean velocity. To a first approximation, it can be considered that 3.2 cm represents the minimum height of successful entry into the flight tube and 5.2 cm the maximum height. Under these guidelines, calculations were performed for the optimum delay times (mean velocities) for Al^+, Eu^+, and C_{60}^+. From Table III.15, the 3.2 cm to 5.2 cm difference encompasses possible velocities of 4444 to 7222 m/s, 1488 to 2418 m/s, and 710 to 1153 m/s for Al^+, Eu^+, and C_{60}^+, respectively. The true velocity spread could therefore be narrowed when the range of possible heights of successful entrance into the flight tube is considered.

Table III. 15: Velocity range as flight tube entrance height is considered.

SPECIES	**Velocity Range (m/s)**		**Energy x 10^{-19} J**	
	3.2 cm	**5.2 cm**	**3.2 cm**	**5.2 cm**
Al^+	4444	7222	4.48 (2.80 eV)	11.6 (7.26 eV)
Eu^+	1488	2418	2.82 (1.76 eV)	7.30 (4.57 eV)
C_{60}^+	710	1153	2.99 (1.86 eV)	7.97 (4.98 eV)

III.7.5.-- Practical implications of the differences in ablation velocity for different analytes

For practical instrumental operation, such differences in velocity from species to species must be taken into account to select proper extraction pulse delay times. From Table III.11, it is clear that attempting to analyze a wide range of masses simultaneously may be problematic because of the extraction time dependence on mass. Since Al^+ was not extracted at all for pulse delays above about 11 microseconds and the fullerenes were not successfully entering the flight tube for delays under about 35 microseconds, these two species would be difficult to investigate in a single spectrum. Similarly, maximization of the intensity for one particular ion could lead to false predictions about the relative abundance of two or more ions. To correct for this, one possibility is to record spectra at the optimum delay times for the variety of species to be studied. This procedure, however, is more time-consuming than a single-condition spectrum, and may also suffer from abundance fluctuations due to variations in laser intensity beam focus.

The specificity of optimum extraction pulse delay times for different masses, however, does indeed have clear advantages. Should the relative abundance of one particular sample component dominate the observed spectrum so much as to obscure other masses, the extraction delay time can be adjusted away from the optimum of the most intense species. One such example is depicted in the case of the 0.033% Eu:CaO sample which was analyzed. The most intense peak, occurring at 28.50 μs, corresponds to the most abundant calcium isotope, $^{40}Ca^+$. In the first spectrum (Figure III.12), the optimum delay time is maximized for $^{40}Ca^+$, and clearly this signal swamps nearby masses, saturates the detector, and prohibits resolution of isotopes with similar times of flight. In addition, the $^{40}Ca^+$ peak itself suffers from extreme broadness making the determination of the time-of-flight inexact. However, by increasing the delay time (Figure III.13), the $^{40}Ca^+$ signal is brought on-scale and resolution is increased to over 400 for the $^{40}Ca^+$ species without adjusting any other parameters. Furthermore, the Ca^+ isotopes which were obscured in Figure III.12 are now cleanly separated from the $^{40}Ca^+$ and visible at 29.20 μseconds ($^{42}Ca^+$) and 29.88 μseconds ($^{44}Ca^+$). Resolution of nearby masses was achieved by attenuating the most abundant peak without decreasing the laser intensity to the point of making trace components indistinguishable from the baseline. Moreover, there is the possibility of increasing the detector gain to detect trace ions that, although not directly obscured by the most abundant peak, are below the S/N of the instrument. Operating at delay times away from the optimum for the most abundant ion thus enhances the signal and improves the limits of detection, and the of the optimum extraction delay time can be used advantageously.

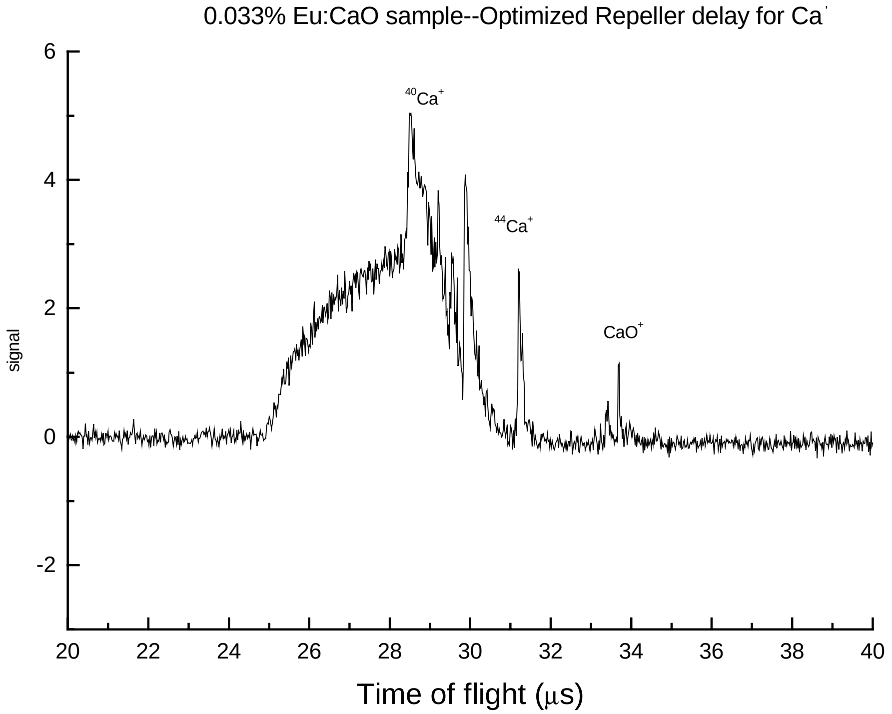

Figure III. 12: Signal saturation and loss of resolution as repeller delay is optimized for the Ca$^+$ peak.

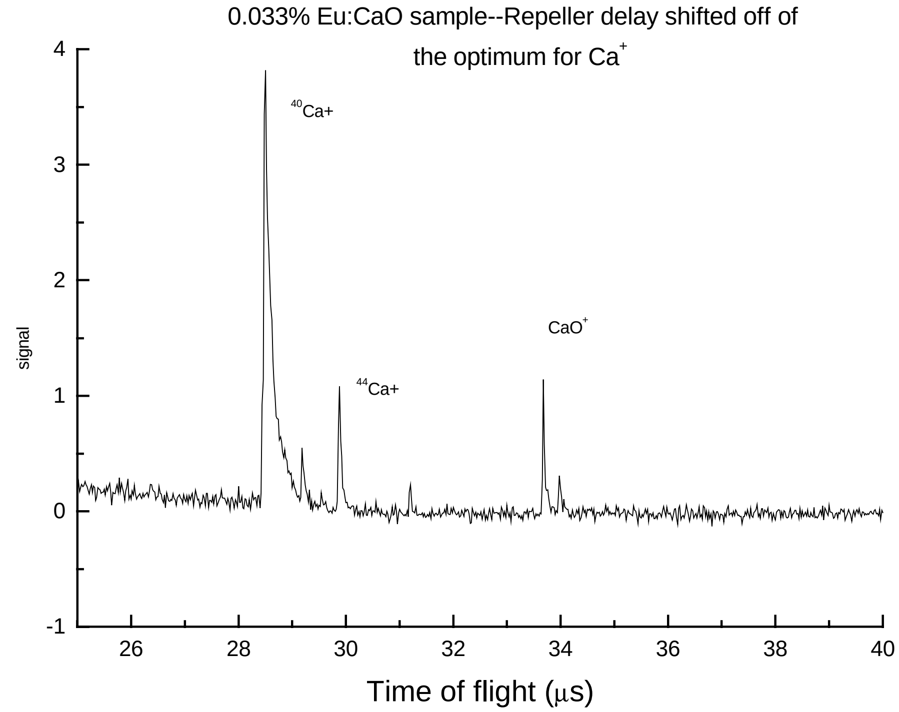

Figure III. 13: Increased resolution as the repeller delay is shifted from .